Lawrence Berkeley National Laboratory
Lawrence Berkeley National Laboratory

Title

Preparations for EUV interferometry of the 0.3 NA MET optic

Permalink
https://escholarship.org/uc/item/0nt0x5bv

Authors
Goldberg, Kenneth A.
Naulleau, Patrick P.
Denham, Paul E.
et al.

Publication Date
2003-10-30

eScholarship.org Powered by the California Digital Library
University of California

Preparations for EUV Interferometry of the 0.3 NA MET Optic

Kenneth A. Goldberg, Patrick P. Naulleau, Paul E. Denham, Senajith B. Rekawa,
Keith H. Jackson, J. Alexander Liddle, Bruce Harteneck, Eric Gullikson, Erik H. Anderson
Center for X-Ray Optics, Lawrence Berkeley National Laboratory, Berkeley, CA 94720

An at-wavelength interferometer is being created for the measurement and alignment of the 0.3 numerical aperture Micro Exposure Tool projection optic at EUV wavelengths. The prototype MET system promises to provide early learning from EUV lithographic imaging down to 20-nm feature size. The threefold increase to 0.3 NA in the image-side numerical aperture presents several challenges for the extension of ultra-high-accuracy interferometry, including pinhole fabrication and the calibration and removal of systematic error sources.

Keywords: interferometry, extreme ultraviolet lithography, EUV, at-wavelength testing, MET.

I. INTRODUCTION

EUV projection optical systems operating near 13-nm wavelength require sub-nanometer system wavefront performance to achieve diffraction-limited imaging.[1] At this time, interferometry with sufficiently high accuracy for EUV optical testing and alignment is not widely available. Furthermore, as the numerical aperture (NA) of prototype EUV optics is extended from 0.1 in the previous generation to 0.3 in the latest, the challenge of high accuracy increases by several-fold.

High-accuracy interferometry is a cornerstone requirement for the success of EUV optical systems. Interferometer absolute accuracies in the 50 pm range are a requirement for the measurement of production-quality EUV elements and assembled systems.[1] State-of-the-art visible-light testing is used in the fabrication of the individual mirror elements[2,3] and has been used in the alignment of numerous assembled EUV optical systems.[4,5,6]

Visible-light interferometry continues to benefit by close, ongoing comparisons with EUV interferometric measurements performed on the same optical systems. A system-level comparison performed at more than 40 points across the field of view of the Engineering Test

Stand (ETS) Set-2 optic, revealed a level of agreement of 0.35±0.11 nm between EUV and visible light interferometries.[7] The discrepancy was concentrated in the lowest spatial frequency aberrations (astigmatism in particular) which are most important for system alignment. Several systematic measurement error sources have been identified via comparison, and were addressed in subsequent visible-light measurements.

Measurements performed at the operational EUV wavelengths, *at-wavelength*, remove potential uncertainties about the response of the resonant-reflective multilayer coatings, and have provided accurate predictions of imaging performance.[8] Relative to visible-light interferometry, the considerably shorter EUV wavelength reduces the length scale of reference and simplifies many aspects of interferometric measurement. EUV interferometry has been used in the diagnosis and remediation of several types of fabrication and system-alignment errors, in the assessment of chromatic effects[9] and flare,[10] and most importantly, in the optimization of imaging performance.

EUV interferometry performed with the phase-shifting point diffraction interferometer (PS/PDI)[11,12] has demonstrated accuracy levels of 40-70 pm during the testing of previous generations of prototype EUV optical systems, typically of 0.08–0.10 NA, developed for EUV lithography research.[13] Prior to measurements with the PS/PDI, the optics are measured with lateral shearing interferometry (LSI) which is performed with a cross-grating transmission beamsplitter placed near the image-plane.[14] As reported previously, for the initial measurement of a nominally pre-aligned test optic, the LSI has several advantages over the PS/PDI. These include ease of alignment, high efficiency, and the potential to measure aberrations of larger magnitudes. Switching between the PS/PDI and the LSI requires only a change of the image-plane mask. To accommodate image-plane mask changes, the experimental chamber is equipped with a manual transfer port. This same port also supports the vacuum load-lock wafer transfer system used when the system is operated in its printing configuration.

In pursuit of early learning with EUV prototype projection imaging systems having sub-30-nm resolution, a new generation of 0.3 NA Micro Exposure Tools (MET) is being

created.[15] The MET optics have an annular pupil; the design has a convex primary mirror and a larger, concave secondary mirror. One such system is being developed on an undulator beamline at Lawrence Berkeley National Laboratory's (LBNL) Advanced Light Source (ALS). Prior to static microfield imaging experiments, the projection optic will undergo an array of at-wavelength tests including EUV interferometry using point-diffraction and lateral shearing techniques.

There are several areas where the extension of interferometry to 0.3 NA poses significant challenges. Perhaps the foremost challenge is the fabrication and use of appropriately sized pinhole spatial filters, which are responsible for producing the nearly perfect spherical reference waves in the object (mask) and image (wafer) planes. The testing geometry also necessitates appropriate calibration of the interferometer to remove systematic aberrations.

The mirror substrates of the 2-mirror, 5×, MET optic that will be measured at Berkeley were fabricated by Carl Zeiss. Molybdenum-silicon multilayer coatings were applied at Lawrence Livermore National Laboratory (LLNL) in close collaboration with at-wavelength reflectometry performed at LBNL. A lensless, visible-light, phase-shifting diffraction interferometer (PSDI) at LLNL[16] was used to align and optimize the wavefront quality of the MET. A visible-light system wavefront measurement is shown in Fig. 3. On the reduced annular range between 10 and 26 mm diameter (the full pupil spans 8.4–27 mm), a fit to the first 37 annular Zernike polynomials yields an RMS wavefront aberration magnitude of 0.56 nm ($\lambda_{EUV}/24$).

II. INTERFEROMETER DESIGN

At EUV wavelengths where well-characterized reference optics are not available and short-coherence lengths are the rule, common-path interferometers have proven successful. Diffraction from sub-resolution pinhole apertures in opaque free-standing absorber membranes is used to produce nearly perfect spherical reference waves covering the measurement solid angles. The elimination of re-imaging optics to combat diffraction, and complex numerical propagation calculations in the data analysis is made possible by the relatively short EUV wavelengths, thus removing two potential measurement error sources.

The details of the new interferometer design, described previously,[16] follow the design of previously reported PS/PDIs[18,19] with components scaled or modified to accommodate the higher NA and resolution of the MET optical system. The interferometer is designed to perform wavefront measurements at multiple points across the 200 × 600 μm image-side field of view, including the longitudinal direction. Light enters the MET vertically from above: the illuminating beam is aligned to coincide with the optic axis. Figure 2 is a mechanical drawing showing how the MET is supported within the vacuum chamber.

The interferometer operates on an undulator beamline optimized for high coherent flux near 13-nm wavelength; this beamline has been used for all previous interferometry of reflective EUV optical systems performed by the Center for X-Ray Optics.[20,21] An adjustable Kirkpatrick-Baez (K-B) mirror pair focuses the synchrotron beam into the object plane of the test optic with a numerical aperture of approximately 0.006 NA.[22]

High-resolution object- and image-plane stages support pinhole arrays and provide five degrees of freedom (x, y, z, θ_x, and θ_y). These stages are mounted to a common support structure that moves with the test optic as a single unit on a vibration isolated planar bearing stage. The optic and its conjugate-plane stages move beneath the stationary illuminating beam.

A meaningful comparison of EUV and visible-light system wavefront measurements requires accurate knowledge of the conjugate point positions with respect to the optical housing of the MET. To achieve a relative wavefront accuracy of 50 pm or below, the field position tolerance is 125 μm laterally and 8 μm longitudinally. A kinematically positioned *metrology tower* supporting several capacitance micrometers and two in-vacuum CCD[23] cameras below the object plane, is used to transfer the measured conjugate point positions from the visible-light interferometer to the EUV interferometer.

A retractable multi-purpose stage below the object plane holds a coarse (66-μm pitch) transmission diffraction grating beam splitter for the PS/PDI and a photodiode to help align the illuminating beam through pinholes in the object plane. This stage enables fine grating motion (for phase-shifting) in addition to grating rotation and longitudinal translation (to control the

image-plane beam-separation direction and magnitude). A photodiode also mounted on this stage helps to align the illuminating beam through pinholes in the object plane pinhole array.

Below the MET, a back-thinned, back-illuminated EUV CCD camera with one-square-inch area faces upward. The CCD camera has 1024 × 1024 square pixels and is thermoelectrically cooled to approximately –35°C. The camera is stationary; in order to capture the full pupil and accommodate the translation of the test optic, the detector plane of the CCD is positioned one inch below the image plane.

The experimental chamber, originally designed for the measurement of the larger, ETS projection optics, maintains a vacuum environment at base pressures in the range of 10^{-7} Torr. Although the chamber cannot be baked, strict adherence to UHV practices is observed and only compatible materials are used in the fabrication. Situated at the beamline, a thermally insulated, temperature controlled enclosure surrounds the system.

A. Pinhole masks

Open stencil pinhole masks comprised of a free-standing Ni absorber membrane are used in both the object- and image-planes of the interferometer. The pinhole masks used in the PS/PDI are fabricated with electron-beam lithography using LBNL's *Nanowriter* electron-beam lithography tool.[24] The PS/PDI and LSI share an object-plane mask whose design facilitates measurement at nine field points arranged in a 3 × 3 grid spanning 1 × 3-mm on a single membrane. The pinhole sizes appropriate for the 0.06 input NA of the MET are between 100 and 200-nm diameter. The focal spot of the beamline's K-B mirror pair is approximately 10 × 20 μm FWHM, significantly larger than the object-plane pinholes. To block the unwanted light, the Ni absorber membrane is given a 250-nm thickness. A pinhole-to-pinhole separation of 80 μm ensures that only one mask pinhole will be illuminated at a time. At each of the nine field points is a similar array pinholes with a variety of sizes so that the optimal size can be selected experimentally. At several locations, pairs of pinholes oriented in various directions serve as unabmiguous alignment marks for identifying the beam's position within the array.

For LSI measurements,[14] a 25%-open square-grid grating made from a Ni absorber on a silicon-nitride membrane is used as the beamplitter. The grating is positioned longitudinally so the image-plane will lie in a Talbot plane, or self-focusing plane, of the grating. The Talbot plane positions, given approximately by nd^2/λ (n is a small integer, d is the grating pitch, and λ is the wavelength), guarantee high-contrast fringes.[25] Typically, a Talbot plane is selected where the grating produces 40–150 fringes across the pupil (in two directions). The grating pitch determines the magnitude of the shear, and hence the sensitivity of the measurement. Four different grating sizes are fabricated side-by-side on the same membrane, so the optimal grating pitch can be chosen experimentally. Furthermore, measurements can be made with different shear ratios to reduce the measurement uncertainty.

The PS/PDI requires a special image-plane mask containing larger "windows" adjacent to pinholes. While the test beam passes through the window and preserves the wavefront aberrations, the reference beam is focused onto a pinhole to generate a second spherical reference wave through diffraction. To achieve a fringe density of approximately 60 fringes across the pupil, a 1.7 μm image-plane beam separation was chosen. The windows are 1-μm wide with unique identifying features along two sides.[26] In addition, each window has two adjacent pinholes for measurements with a 90° rotation in the beam-separation direction. As with the object pinhole mask, the image-plane mask features are arrayed with various pinhole sizes and a large redundancy of pinholes, in addition to distinct alignment marks.

B. Pinhole development and testing.

The accuracy of the PS/PDI interferometer relies on the quality of the spherical reference waves diffracted by pinholes whose diameters are only 2–15 times the wavelength of EUV light. To diffract a spherical wave broad enough to cover the solid angle of measurement, the pinhole sizes are chosen approximately equal to or smaller than the diffraction-limited resolution of the test optic. While the quality of the diffracted wavefronts generally improves with decreasing pinhole size, the accompanying reduction in transmitted power necessitates a compromise between pinhole size and wavefront quality.[27]

In the object plane, appropriately sized pinholes for the 0.06 input NA of the MET are expected to be 120–160 nm in diameter. This is larger than the 80–120 nm image-plane pinholes used in the measurement of 0.1 NA optics in the past. Simulations of pinhole diffraction with TEMPEST3D[28] (a time-domain vector electromagnetic field simulation program) show that for parameters like diffraction intensity FWHM and total transmitted power, pinholes of this size behave in a manner that is well described by simple, thin-screen scalar diffraction theory.

For both fabrication and diffraction analysis, appropriately sized image-plane pinholes present greater difficulties. Here the pinhole diameters of interest fall in the 25–50-nm range. To maintain a high opacity to block the weakly-transmitted test beam, the Ni absorber thicknesses must remain above approximately 100 nm—the aspect ratio of the pinholes can be as high as 4:1. TEMPEST models predict a rapid fall-off in the transmitted power through the pinholes as the diameter shrinks below 35 nm.

In preparation for MET interferometry, pinhole fabrication and diffraction experiments have been conducted on a range of pinhole sizes to determine optimal fabrication conditions. Diffraction measurements were made from densely-spaced arrays of nominally identical pinholes collectively illuminated with a collimated beam in ALS beamline 6.3.2: a small-area photodiode was scanned in angle through the diffraction pattern. For pinholes diameters in the range 100–200 nm, a 2 μm grid was used. For pinholes having 20–55-nm diameter, a 500-nm grid spacing was used. Typical diffraction patterns are shown in Figs. 4(a) and (b). While the comb pattern comes from the array spacing, the envelope function reveals the aggregate single-pinhole diffraction pattern. The *apparent size* of the pinholes is established by fitting the measured diffraction pattern to an ideal circular pinhole's "Airy pattern." The apparent sizes are then used to calibrate the pinhole fabrication processes.

Figures 4(c) shows a comparison of the apparent pinhole size (based on diffraction measurements) to the programmed size, for pinholes below 55-nm diameter in a free-standing 80-nm-thick Ni absorber membrane. For the sub-60-nm pinholes, there is a bias of approximately 5 nm: the pinholes diffract as though they are slightly larger than they are

designed to be. Possible explanations include the limitations of the SEM measurements, non-normal placement in the SEM leading to size underestimation, possibly flared pinhole bore shape

For pinholes sizes between 100 and 200-nm, Fig. 3(d) shows the apparent size compared with an average of pinhole sizes measured in a scanning electron microscope (SEM). (In the SEM measurements, the geometric mean of the *x* and *y* pinhole widths were averaged for four or five pinholes at each size.) Here the bias is somewhat larger: for pinholes with diameters between 100- and 160-nm, the pinholes diffract as though they are 20 nm larger than they appear in the SEM. One explanation may be that the pinholes are not perfectly cylindrical. The SEM might see the pinholes' sizes at their narrowest point, while their average diameters may be somewhat larger.

With the inclusion of absorber thickness effects in the pinhole diffraction models, TEMPEST predicts different results from the larger and the smaller pinholes, assuming cylindrical pinhole shapes. The apparent size based on diffraction is predicted to be smaller than the actual size when the pinholes are large and the aspect ratio is above 1:1. This behavior has not been confirmed through experiment. However, for the smallest pinholes under consideration, those below 30 nm, the light diffracted to large angles appears to be attenuated in the absorber membrane, limiting the diffraction angle and making the pinholes appear larger than they are.

The most important outcome of the diffraction measurements was the demonstration that pinholes with sufficiently small size and sufficiently large diffraction angles for PS/PDI interferometry could be produced in the *Nanowriter*. Ongoing research, may seek to improve the agreement between TEMPEST modeling and experimental data.

III. GEOMETRIC CONSIDERATIONS

Unlike many conventional interferometers, the PS/PDI and LSI employed for at-wavelength testing have no optical elements between the image-plane and the CCD detector. The predictable geometric path length difference between the test and the reference beams, propagating to the detector plane from displaced positions in the image-plane, accounts for a compensable systematic measurement error in the interferometer.[27]

The magnitude of the geometric aberration terms, which are dominated by coma, is expected to be on the order of 3 nm RMS. There is an additional sensitivity of the measured astigmatism to the tilt of the detector plane of approximately 0.6 nm RMS per degree of tilt.

To measure and accurately compensate these systematic aberrations, our PS/PDI testing procedure includes the rotation of the image-plane beam-separation direction, which is controlled by the rotation of the beamsplitter grating.[27] Since the magnitudes and orientations of many of the systematic aberrations follow the beam-separation vector, this rotation can be used to isolate the systematic error terms from the wavefront under test.

Error sensitivities in the LSI are somewhat different than the PS/PDI. Measurements are highly sensitive to the tilt of the diffraction grating. In situ measurement (and compensation) of the grating slope can be performed by looking at the changes in wavefront tilt components as the grating is translated, and as the illumination is moved field point to field point. Also in the LSI, small errors or uncertainties in the gradient measurements can lead to much larger errors and uncertainties in the test wavefront, owing to the nature of the aberration polynomial derivatives.

In addition to the aberrations that arise form the beam-separation, the projection of the spherical pupil wavefront onto a planar detector results in a radial distortion that must be compensated in the wavefront measurement. In previous measurements of EUV optical systems with NA values of 0.1 and below, the radial distortion magnitudes were limited to a fraction of a detector pixel. At 0.3 NA, with 600 pixels in the diameter of the measurement domain, the peak distortion will be approximately 3 pixels.[27] At EUV wavelengths, diffraction (from the baffles, pupil apertures and potential imperfections on the mirror surfaces) is spatially localized obviating the necessity of numerical propagation calculations to re-create the wavefront in the exit pupil of the test optic.

IV. SUMMARY

EUV interferometric testing of the 0.3 NA MET projection optic is being performed on undulator beamline 12.0.1 of the Advanced Light Source at Lawrence Berkeley National Laboratory. Experimental systems and optical elements have been designed to enable lateral

shearing interferometry and phase-shifting point diffraction interferometry at points spanning the three-dimensional field of view. Among the technical challenges of working at higher numerical aperture than previous EUV interferometers are the fabrication and use of sub-50-nm pinholes, and the measurement and compensation of NA-dependent geometric systematic errors.

ACKNOWLEDGMENTS

The authors are grateful for the contributions of CXRO members including Kevin Bradley, Brian Hoef, René Delano, Ronald Oort, C. Drew Kemp, M. Gideon Jones, Ronald Tackaberry, Robert Gunion, and David Attwood; and from LLNL, John Taylor, Gary Sommargren, Don Phillion, Mike Johnson, Carl Chung, Layton Hale, Henry Chapman, and Donald Sweeney.

This work is funded by International Sematech, and the EUV Limited Liability Corporation (EUV LLC).

1. D. Sweeney, Proc. SPIE 5037, *to be published*.
2. G. E. Sommargren, U.S. Patent 5,548,403, August 20, 1996.
3. H. N. Chapman and D. W. Sweeney, Proc. SPIE **3331**, 102 (1998).
4. K. A. Goldberg, P. Naulleau, S. H. Lee, C. Chang, *et al.*, Proc. SPIE **3676**, 635 (1999).
5. D. A. Tichenor, G. D. Kubiak, W. C. Replogle, L. E. Klebanoff, *et al.*, Proc. SPIE **3997**, 48 (2000).
6. K. A. Goldberg, P. Naulleau, J. Bokor, and H. N. Chapman, Proc. SPIE **4688**, 329 (2002).
7. K. Goldberg, P. Naulleau, J. Bokor and H. Chapman, J. Vac. Sci. & Technol. B **20**, 2834 (2002).
8. P. Naulleau, K. A. Goldberg, E. Anderson, D. Attwood, *et al.*, J. Vac. Sci. & Technol. B **20**, 2829 (2002).
9. E. Tejnil, K. A. Goldberg, J. Bokor, Applied Optics **37**, 8021 (1998).
10. P. Naulleau, K. A. Goldberg, E. M. Gullikson, and J. Bokor, J. Vac. Sci. & Technol. B **17**, 2987 (1999).
11. H. Medecki, U.S. Patent No. 5,835,217, November 10, 1998.
12. H. Medecki, E. Tejnil, K. A. Goldberg, and J. Bokor, Opt. Lett. **21**, 1526 (1996).

13. P. P. Naulleau, K. A. Goldberg, S. H. Lee, C. Chang, D. Attwood, and J. Bokor, Appl. Opt. **38**, 7252 (1999).
14. P. P. Naulleau, K. A. Goldberg and J. Bokor, J. Vac. Sci. & Technol. B **18**, 2939 (2000).
15. R. Hudyma, LLNL Internal Report M199900286, September 24, 1999.
16. G. E. Sommargren, D. W. Phillion, M. A. Johnson, N. Q. Nguyen, A. Barty, F. J. Snell, D. R. Dillon, L. S. Bradsher, Proc SPIE **4688**, 316 (2002).
17. K. A. Goldberg, P. Naulleau, P. Denham, S. B. Rekawa, K. Jackson, E. H. Anderson, J. A. Liddle, J. Bokor, Proc. SPIE **5037**, *to be published.*
18. K. A. Goldberg, E. Tejnil, S. H. Lee, H. Medecki, *et al.*, Proc. SPIE **3048**, 264 (1997).
19. K. A. Goldberg, P. Naulleau, P. Batson, P. Denham, H. Chapman, and J. Bokor, J. Vac. Sci. & Technol. B **18**, 2911 (2000).
20. D. T. Attwood, P. Naulleau, K. A. Goldberg, E. Tejnil, *et al.*, IEEE Journal of Quantum Electronics **35**, 709 (1999).
21. R. Beguiristain, J. H. Underwood, M. Koike, P. Batson, *et al.*, Rev. Sci. Instrumen. **67**, 1 (1996).
22. P. P. Naulleau, K. A. Goldberg, P. J. Batson, S. Jeong, and J. H. Underwood, Appl. Opt. **40**, 3703 (2001).
23. P. P. Naulleau, P. J. Batson, P. E. Denham, and M. S. Jones, U.S. Patent No. **6,327,102,** March 7, 2000.
24. E. H. Anderson, D. Olynick, B. Harteneck, E. Veklerov, *et al.*, J. Vac. Sci. & Technol. B **18**, 2970 (2000).
25. D. Malacara, and A. Cornejo, *Bol. Inst. Tonantzintla,* **1**, 193 (1974).
26. K. Goldberg and P. Naulleau, U.S. Patent No. 6,118,535 (2000).
27. K. A. Goldberg, Ph.D. dissertation, Physics Department, Univ. Calif., Berkeley, 1997.
28. A. K. Wong, A. R. Neureuther, IEEE Transactions on Semiconductor Manufacturing **8**, 419 (1995).

Figure Captions

Fig 1. The MET optical system resting on a stand. Photo courtesy of John Taylor, LLNL.

Fig 2. Mechanical drawing of the interior components of the experimental test chamber configured for MET measurement. At right is an expanded view of the MET as it is held in an annular support ring. Object and image-plane components are shown schematically.

Fig 3. Visible-light wavefront measurement of the MET, courtesy of Don Phillion, LLNL. The full annular pupil size is indicated by the dashed lines. A single arm supports a central stop and obstructs a portion of the annulus.

Fig 4. Diffraction measurements performed on dense arrays of nominally identical pinholes during the development of pinhole fabrication techniques. Typical diffraction patterns from (a) 35-nm pinholes with 0.5 μm grid spacing, (b) 160-nm pinholes with 2 μm grid spacing. A solid black line connects the closely-spaced diffraction peaks revealing the aggregate single-pinhole diffraction envelope functions. (c) For sub-60-nm pinholes, the apparent size, based on diffraction measurements, is plotted versus the programmed size. (d) For 100–200-nm pinholes, the apparent size is plotted against the average size of pinholes measured in an SEM.

Fig 1. Photo of the MET optical system resting on a stand. Photo courtesy of John Taylor, LLNL.

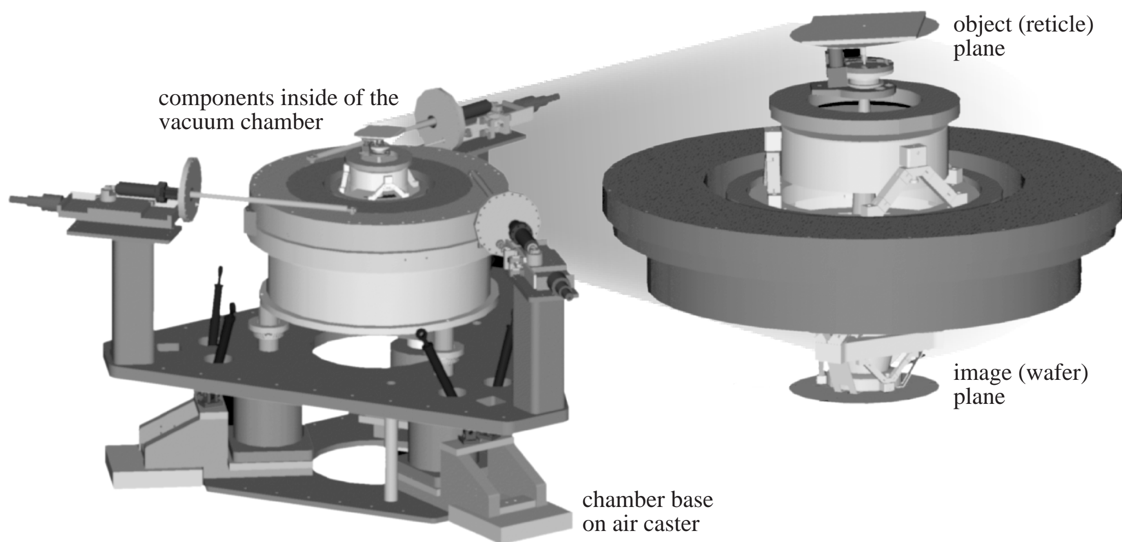

Fig 2. Mechanical drawing of the interior components of the experimental test chamber configured for MET measurement. At right is an expanded view of the MET as it is held in an annular support ring. Object and image-plane components are shown schematically.

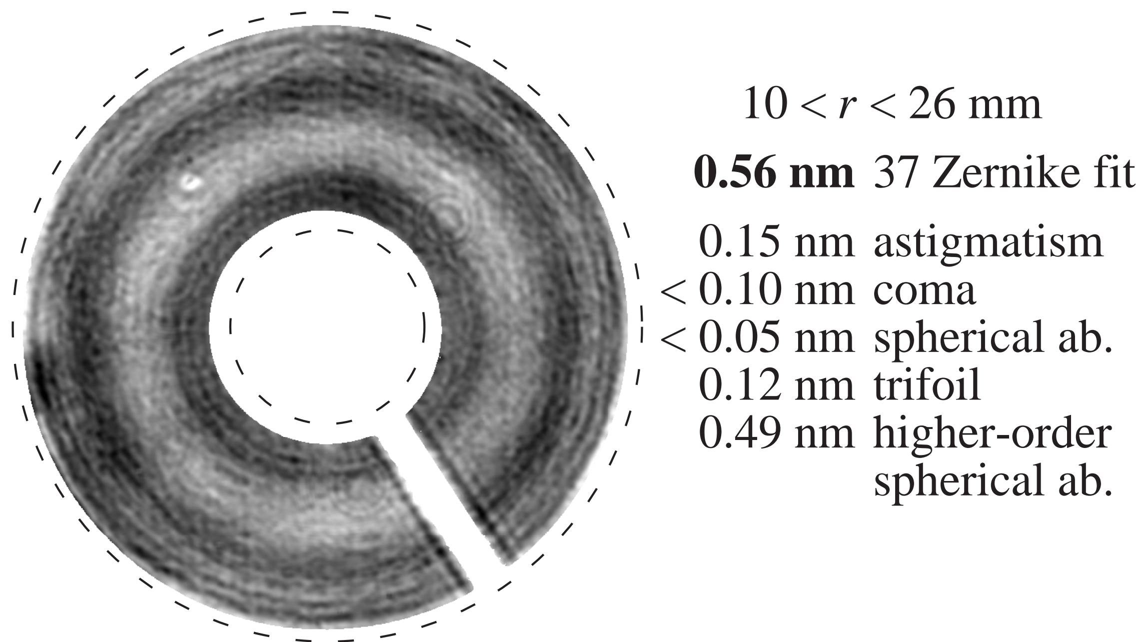

Fig 3. Visible-light wavefront measurement of the MET, courtesy of Don Phillion, LLNL. The full annular pupil is indicated by the dashed lines and subtends a radius from 8 to 27.5 mm. Here, a single arm supports a central stop and obstructs a portion of the annulus.

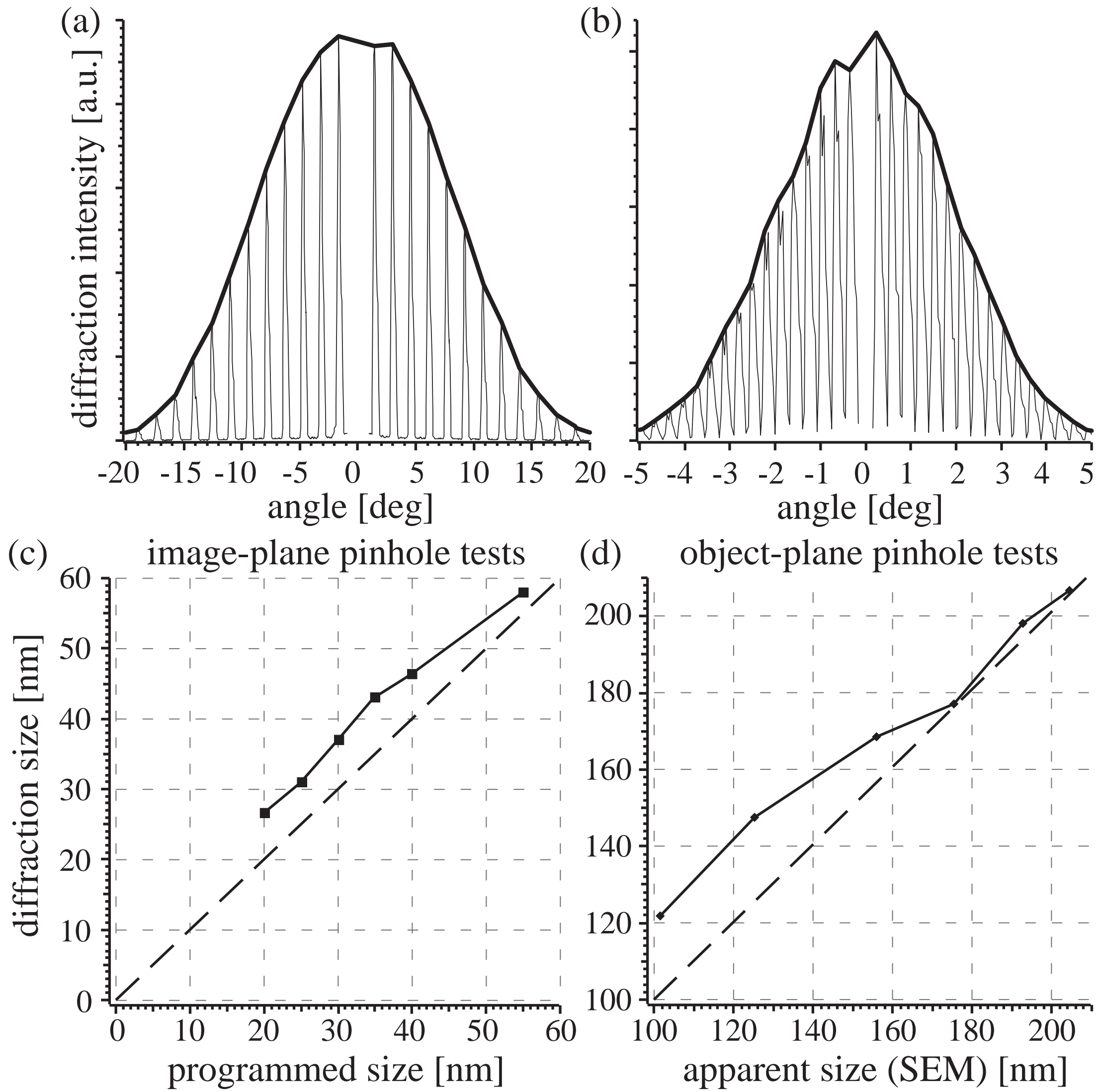

Fig 4. Diffraction measurements performed on dense arrays of nominally identical pinholes during the development of pinhole fabrication techniques. Typical diffraction patterns from (a) 35-nm pinholes with 0.5 μm grid spacing, (b) 160-nm pinholes with 2 μm grid spacing. A solid black line connects the closely-spaced diffraction peaks revealing the aggregate single-pinhole diffraction envelope functions. (c) For sub-60-nm pinholes, the apparent size, based on diffraction measurements, is plotted versus the programmed size. (d) For 100–200-nm pinholes, the apparent size is plotted against the average size of pinholes measured in an SEM.